Soft Matter

# The Effect of Rigid Cells on Blood Viscosity: Linking Rheology and Sickle Cell Anemia



| | |
|---|---|
| Journal: | *Soft Matter* |
| Manuscript ID | SM-ART-09-2021-001299.R1 |
| Article Type: | Paper |
| Date Submitted by the Author: | 27-Nov-2021 |
| Complete List of Authors: | Perazzo, Antonio; Princeton University, Mechanical and Aerospace Engineering; Princeton University<br>Peng, Zhangli; University of Illinois at Chicago, Department of Bioengineering<br>Young, Yuan-Nan; New Jersey Institute of Technology, Mathematical Sciences<br>Feng, Zhe; University of Illinois at Chicago, Department of Bioengineering<br>Wood, David; University of Minnesota, Biomedical Engineering<br>Higgins, John; Harvard University, Systems Biology<br>Stone, Howard; Princeton, Mechanical and Aerospace Engineering |
| | |

Soft Matter

ARTICLE TYPE

Cite this: DOI: 10.1039/xxxxxxxxxx

# The Effect of Rigid Cells on Blood Viscosity: Linking Rheology and Sickle Cell Anemia†

Antonio Perazzo,[a,b,c] Zhangli Peng,[d] Y.-N. Young,[e] Zhe Feng,[d] David K. Wood,[f] John M. Higgins [g] and Howard A. Stone *[c]

Received Date
Accepted Date

DOI: 10.1039/xxxxxxxxxx

www.rsc.org/journalname

Sickle cell anemia (SCA) is a disease that affects red blood cells (RBCs). Healthy RBCs are highly deformable objects that under flow can penetrate blood capillaries smaller than their typical size. In SCA there is an impaired deformability of some cells, which are much stiffer and with a different shape than healthy cells, and thereby affect regular blood flow. It is known that blood from patients with SCA has a higher viscosity than normal blood. However, it is unclear how the rigidity of cells is related to the viscosity of blood, in part because SCA patients are often treated with transfusions of variable amounts of normal RBCs and only a fraction of cells will be stiff. Here, we report systematic experimental measurements of the viscosity of a suspension varying the fraction of rigid particles within a suspension of healthy cells. We also perform systematic numerical simulations of a similar mixed suspension of soft RBCs, rigid particles, and their hydrodynamic interactions. Our results show that there is a rheological signature within blood viscosity to clearly identify the fraction of rigidified cells among healthy deformable cells down to a 5% volume fraction of rigidified cells. Although aggregation of RBCs is known to affect blood rheology at low shear rates, and our simulations mimic this effect via an adhesion potential, we show that such adhesion, or aggregation, is unlikely to provide a physical rationalization for the viscosity increase observed in the experiments at moderate shear rates due to rigidified cells. Through numerical simulations, we also highlight that most of the viscosity increase of the suspension is due to the rigidity of the particles rather than their sickled or spherical shape. Our results are relevant to better characterize SCA, provide useful insights relevant to rheological consequences of blood transfusions, and, more generally, extend to the rheology of mixed suspensions having particles with different rigidities, as well as offering possibilities for developments in the field of soft material composites.

## 1 Introduction

Blood is a fluid that has a viscosity dependent on the volume fraction or hematocrit of red blood cells (RBCs), their deformability,

[a] Novaflux Inc., Princeton, NJ 08540
[b] Advanced BioDevices LLC, Princeton, NJ 08540
[c] Department of Mechanical and Aerospace Engineering, Princeton University, Princeton, NJ 08544
[d] Department of Biomedical Engineering, University of Illinois at Chicago, Chicago, IL 60607
[e] Department of Mathematical Sciences, New Jersey Institute of Technology, Newark, NJ 07102
[f] Department of Biomedical Engineering, University of Minnesota, Minneapolis, MN 55455
[g] Center for Systems Biology and Department of Pathology, Massachusetts General Hospital, and Department of Systems Biology, Harvard Medical School Boston, MA 02114

† Electronic Supplementary Information (ESI) available: [details of any supplementary information available should be included here]. See DOI: 10.1039/cXsm00000x/

‡ Additional footnotes to the title and authors can be included *e.g.* 'Present address:' or 'These authors contributed equally to this work' as above using the symbols: ‡, §, and ¶. Please place the appropriate symbol next to the author's name and include a `\footnotetext` entry in the the correct place in the list.

shape, tendency to aggregate and the velocity gradient at which blood is flowing[1–3]. RBCs are deformable biconcave disks approximately eight microns long and two microns thick that can move into narrow blood conduits, at least as small as five microns, thereby often assuming a parachute-like shape or an asymmetric (slipper) shape[4–8]. The relation between the biomechanics of RBCs and the rheology of blood flow has been studied extensively[9–13], e.g., including theoretical modeling and numerical simulations[14,15] and experiments[16]. One of the main challenges in studying the biomechanics of RBC flow is the physiologically relevant range of RBC volume fraction in blood[17]: in the main arteries of healthy humans the hematocrit in blood is around 45% volume fraction. Even in small blood vessels the volume fraction of RBCs is typically not smaller than 20%, so that it is difficult to understand the blood rheology by inferring results from knowledge of dilute suspensions.

It has long been known that in patients affected by sickle cell anemia (SCA) there is an increase in blood viscosity that is related to the reduced deformability of RBCs. In particular, the diseased cells are observed to have increased rigidity and an altered shape. Both of these changes are a function of the rate of blood deoxygenation and originate from a genetic mutation that produces abnormal hemoglobin. The increase in viscosity of SCA-affected blood has been detected using direct rheometrical measurements and in-vitro microfluidic velocimetry experiments[18,19], as well as indicated in simulations[20–24]. However, because diseased blood contains both healthy and diseased cells, the macroscopic rheology measurements necessarily produce some average value for the effective fluid properties. Nevertheless, even recognizing the large body of literature on the mechanics of suspensions, it is unknown what is the effect on blood viscosity of a certain fraction of rigid cells within a population of healthy cells. This lack of knowledge implies poor understanding of the possible rheology of the blood of SCA patients, who are often treated with transfusions containing variable amounts of normal RBCs and only a fraction of the cells will be stiff.

Here, we perform rheometrical measurements and dissipative particle dynamics (DPD) simulations to show that there is an increase in the viscosity of SCA-affected blood, as compared to healthy blood, that allows identification of the approximate fraction of rigidified (i.e., diseased) cells, with a volume fraction as low as 5%, within a population of healthy deformable cells. Specifically, we are referring here to cases where not all cells are rigidified/affected by sickle cell anemia, which is a situation that occurs, for example, after transfusions. These results are relevant to better characterize sickle cell anemia, provide useful insights towards blood transfusions, and, more generally, extend to the rheology of mixed suspensions having particles with different rigidities. Thus, the ideas discussed here should offer possibilities for developments in the field of soft material composites.

To create the mixed suspensions for the experiments we disperse healthy RBCs and spherical PMMA particles (6 microns in diameter) within a population of RBCs derived from healthy human blood (see Methods). In our experiments, the total volume fraction of particles in the suspension, i.e., the sum of healthy RBCs and rigid particles, is always maintained equal to 25% by volume and we document changes in the effective viscosity of the suspension as the ratio of rigid (diseased) and soft (healthy) particles is varied.

Also, we report DPD simulations of a similar mixed suspension and document similar trends in the viscosity variation, as found in the experimental measurements, as a function of the ratio of volume fractions of rigid to soft objects. These results provide one of the first examples of the role of rigidity in the viscosity of a suspension of a mixture of particles. To the best of our knowledge, there are no reports in the literature on suspension rheology for how particles with different elastic moduli contribute to the overall viscosity of a suspension. Our results highlight one way to develop "suspension engineering", where one can imagine designing a specific effective viscosity or modulus of a suspension by varying the particle volume fraction, roughness, size and attraction potentials but also by mixing particles of different elasticities.

In the next section, §II, we describe the experimental and simulation approaches. Then, in §III first we provide the results of our experimental measurements of the rheology of suspensions that is a mixture of healthy red blood cells and rigid particles and second the results of our numerical simulations of these suspensions.

## 2 Materials and methods

### 2.1 Experiments

*Preparation of suspensions:* Healthy human blood with added anticoagulant ACD was obtained from a blood bank (Biological Specialty Corporation, Colmar, Pennsylvania). Here and throughout the manuscript plasma refers to blood without RBCs, i.e., the blood only contains white blood cells, platelets and other small proteins along with plasma. We separated plasma from RBCs by centrifugation at 10,000 rpm for 15 minutes. Once plasma was extracted from the phase-separated solution, we dispersed rigid spherical particles of PMMA, with average diameter 6 microns (Spheromers CA-6, 6M-006-2423, Microbeads AS, Norway), and healthy RBCs in plasma; different ratios of the concentrations of rigid particles and healthy cells were used and the overall volume fractions of RBCs plus rigid particles was always equal to 25%.

*Rheometrical measurements:* Suspension rheometry was performed in a stress-controlled rheometer (Anton Paar Physica MCR 301) at 37°C with a roughened parallel-plate geometry having diameter of 50 mm. Roughened parallel plates were used to minimize wall slip. The gap between the plates was either 0.5 mm or 1 mm as noted below. We performed shear rate ramps and, before changing the shear rate, each shear rate was kept constant for at least 30 seconds. We work with suspensions of 25% volume fraction of particles, which is representative of SCA in vivo[18]. For most of physiological blood flow conditions in small vessels blood shear rates are never higher than 150-200 $s^{-1}$ (with the exception of large vessels[25]), so in our experiments we operate with shear rates less than 100 $s^{-1}$.

We also measured the elastic modulus ($G'$) of the suspensions by small amplitude oscillatory shear rheology (SAOS) and found $G'$ to be negligible. The yield stress was also negligible.

### 2.2 Numerical simulations and setup

The shear viscosity of the suspensions was studied with a RBC model based on the DPD simulation method, which is a particle-based mesoscopic numerical simulation that allows modeling of fluids and soft matter. A DPD system is represented by $N$ particles, which interact through pairwise effective potentials and move according to Newton's second law[26,27]. In a DPD simulation, a particle represents the center of mass of a cluster of atoms or molecules, and the position and momentum of the particle are updated in a continuous phase but spaced at discrete time steps. Particles $i$ and $j$ at positions $\mathbf{r}_i$ and $\mathbf{r}_j$ interact with each other *via* pairwise conservative, dissipative, and random forces. The details of the simulation are provided in the Appendix. The viscous, elastic and total stress tensors were computed based on the virial stress[28]. Also, the shear rate and particle number density were verified to be spatially uniform in the domain during the time of the simulations.

In the RBC model, the membrane is modeled by a two-dimensional triangulated network with $N_v$ vertices, as shown in Fig. S1A, where each vertex is represented by a DPD particle. $N_v = 500$ is used for the current study. The lipid-bilayer has no shear stiffness but only bending stiffness and a very large local area stiffness, whereas the inner layer (cytoskeleton) has no bending stiffness but a large shear stiffness. To generate the shapes of sickled red blood cells, we applied stretching forces at the anchoring points to mimic the force due to intracellular hemoglobin polymerization, which follows the approach in[29]. The sickled cells are then modeled as rigid bodies using the rigid body package in LAMMPS[30]. More details on on how healthy and rigidified RBCs are modeled can be found in §A.4 in the Appendix.

*Simulation setup:* We simulate shear flow of a suspension in a channel. In the simulations, we place about 200 RBCs in linear shear flow between two planar solid walls. The no-slip boundary condition between the fluid and the solid walls, and the coupling between the fluid and the RBC membranes, is enforced using the bounce-back algorithm[23] for particle-based methods. Specifically, the collision between a fluid particle and the surfaces of membranes/walls is calculated at each time step. If the fluid particle penetrates the surface within this step, then its velocity is reversed and its bounce-back position is calculated based on its trajectory. In addition, the viscous friction between the fluid particle and surface particles is adjusted to enforce the no-slip condition[23]. The viscosity of the suspending medium is specified as $\eta_0$ = 0.00134 Pa s based on experimental measurements of human blood plasma[31] and the viscosity of the cytosol inside the RBC is taken as 5 times that of the suspending medium[32] as $\eta_1 = 0.0067$ Pa.s at 37°C.

## 3 Results

In this section we present and compare experimental and simulation results for the effective viscosity of mixtures of healthy and diseased RBCs. In § 3.1 we present experimental measurements of the suspension viscosity as a function of shear rate during shear rate ramps from 1 $s^{-1}$ to 100 $s^{-1}$, with at least 30 seconds between each sequential ramp (see § 3.1). The gap size between the parallel plates of a rheometer is fixed at 1 mm in one set of measurements and reduced to 0.5 mm in another set for comparison: corrections of all experimental data for the shear thinning effect along the plates of the rheometer are made according to Pipe *et al.*[33]; this led to an approximately 20% reduction in the reported viscosity. In § 3.2 we present simulation predictions of the suspension viscosity to compare with the experimental results in § 3.1. The predictions of a model of the effective viscosity of a bimodal suspension, in this case of soft and rigid RBCs, is discussed in § 3.3. Finally, for completeness for understanding the rheological response of an RBC suspension in shear flow, in § 3.4 we numerically investigate the effect of cell-cell adhesion on the suspension viscosity, though we note that with respect to SCA there is no clear evidence that deoxygenation/stiffening increases adhesion.

To emulate the effect of spheroidal rigidified RBCs (typical of SCA) within a suspension of deformable healthy cells in the experiments, we substitute a fraction of RBCs (5%, 10%, 20% of the total suspension volume) with rigid spherical particles of approximately the same surface area as a healthy RBC. In the DPD simulations, we substitute a fraction of RBCs with either rigid spherical particles (of approximately the same surface area as a healthy RBC) or rigid sickled RBCs of the same surface area as the healthy RBCs at the beginning of the simulations.

### 3.1 Rheological measurements of suspensions of RBCs and rigid particles

In the experiments the total volume fraction of RBCs and particles is fixed at 25%. When a fraction of the healthy RBCs is replaced by rigid particles we find an increase in the viscosity at every shear rate, as documented in Figure 1A. Such an increase in viscosity becomes even more pronounced when the ratio of volume fraction of rigid particles to RBCs is higher. The difference in viscosity between suspensions with different volume fractions of rigid particles is reduced at higher shear rates, though it is still significant. For the healthy RBCs, the effect of a small fraction of rigid particles on the suspension is thus as if the healthy cells are immersed in a solvent with a viscosity much higher than the plasma, e.g., we speculate that the viscosity of the solvent experienced by the cells is that of the plasma plus rigid particles. It is known that at these volumetric fractions the viscosity of a suspension of rigid spheres is mostly Newtonian whereas the viscosity of a suspension of RBC and/or deformable cells/droplets is shear thinning. Lanotte et al. reported how the RBC dynamics control the shear thinning behavior of the suspension.[16] Therefore, the shear thinning reported in our measurements and simulations of the mixed suspensions is mostly affected by the healthy/deformable RBC dynamics and the way the solvent (plasma plus rigid particles) affects their dynamics.

We confirm the validity of our results documented in Figure 1A at a lower gap size, i.e., the viscosity always decreases as a function of increasing shear rate but the higher the volume fraction of rigid particles versus soft cells, the higher is the viscosity value at each shear rate (Figure 1B).

There are phenomena possibly affecting the fluid dynamics and

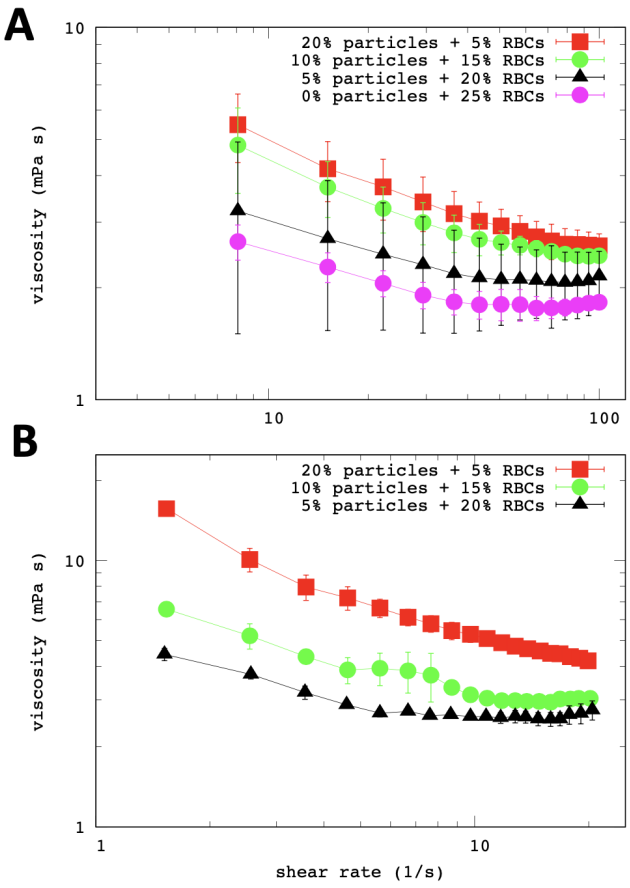


**Fig. 1** Experimental measurements of suspension viscosity using two different gap sizes. (A) Viscosity as a function of the shear rate for suspensions containing healthy RBCs plus spherical rigid particles in plasma. Purple circles: 25% RBCs and no rigid particles, black triangles: 20% RBCs plus 5% rigid particles, green circles: 15% RBCs and 10% rigid particles, and red squares: 5% RBCs and 20% rigid particles. Gap size 1 mm. (B) Viscosity as a function of the shear rate for suspensions containing healthy RBCs plus spherical rigid particles in plasma, similar to (A) but with a smaller measuring gap in the rheometer. Black triangles: 20% volume RBCs plus 5% rigid particles, green circles: 15% RBCs and 10% rigid particles, and red squares: 5% RBCs and 20% rigid particles. Gap size 0.5 mm.

rheometrical measurements of mixtures of particles and cells, such as margination and migration[34–37]. However, margination/migration of cells/particles occurs in 'confined geometries' i.e., when for example in a channel/blood-vessel the diameter of the conduit is less than about 350 microns[38], otherwise there is not sufficient shear rate/shear stress for the phenomenon to occur. Therefore, given that the gap size in the rheometer is significantly larger than 350 microns and given that the maximum shear rates we used were lower than the shear rate needed for migration/margination to occur, we can exclude any margination and wall-depleted layer of particles/cells affecting the rheometrical measurements. In terms of the simulations, we did not notice any cell-free layer effect, which is not surprising given that the shear rates are constant (we used a simple shear flow and not a Poiseuille flow) and are not high enough to induce the effect of a cell-free layer. Concentrated suspensions (where particle concentration $>$ 40% vol) are prone to wall slip, a phenomenon where particles slip at the wall of the measuring geometry of the rheometer. Consequently, there is a reduction in the concentration of particles in the fluid near the walls, and hence lower values of viscosity are measured than in the original suspension. We note though that our suspensions were not so concentrated. Moreover, to limit any possible wall slip effect we used roughened parallel plates as mentioned in § 2.1.

To test whether the gap between the plates had any effect on our measurements, we performed measurements with a smaller gap size (0.5 mm, see Figure 1B). In this case we focused on lower shear rates than in the previous test (shear rate range of the measurements: $2-20$ s$^{-1}$). We note that accessing a broader range of shear rates in a single test would require longer measurement times, which could have resulted in the drying of the RBC suspension at the edge of the sample during the measurements. As can be seen in Figure 1B, even at this different gap size we confirm the validity of our results documented in Figure 1A for the higher gap size, i.e., the viscosity always decreases as a function of increasing shear rate and the higher the volume fraction of rigid particles versus soft cells, the higher is the viscosity value at each shear rate (Figure 1B). The results of Figure 1 make clear the focus of our work of quantifying and rationalizing the effective viscosity of mixtures of healthy and rigid cells, as well as the idea that a fraction of rigid particles in a suspension of healthy (soft) cells can be associated with a specified increase in the suspension viscosity.

### 3.2 Computational prediction of the viscosity as a function of shear rate

To better understand the experimental results in § 3.1 (Figure 1), we conducted dissipative particle dynamics (DPD) simulations of suspensions consisting of rigid particles and deformable healthy RBCs to examine the dependence of viscosity on the shear rate and the ratio of the volume fraction of rigid particles to healthy RBCs in the suspension. In the simulations, we place about 200 healthy RBCs in a linear shear flow between two planar solid walls. First, we varied the volume fractions of the rigid spherical particles (6 $\mu$m in diameter) and RBCs and, similar to the experi-

ments, studied five cases: (I) 20% particles + 5% RBCs; (II) 15% particles + 10% RBCs; (III) 10% particles + 15% RBCs; (IV) 5% particles + 20% RBCs; (V) 0% particles + 25% RBCs. The details of the DPD simulations, the multiscale model of RBCs, and the boundary conditions are provided in the Appendix.

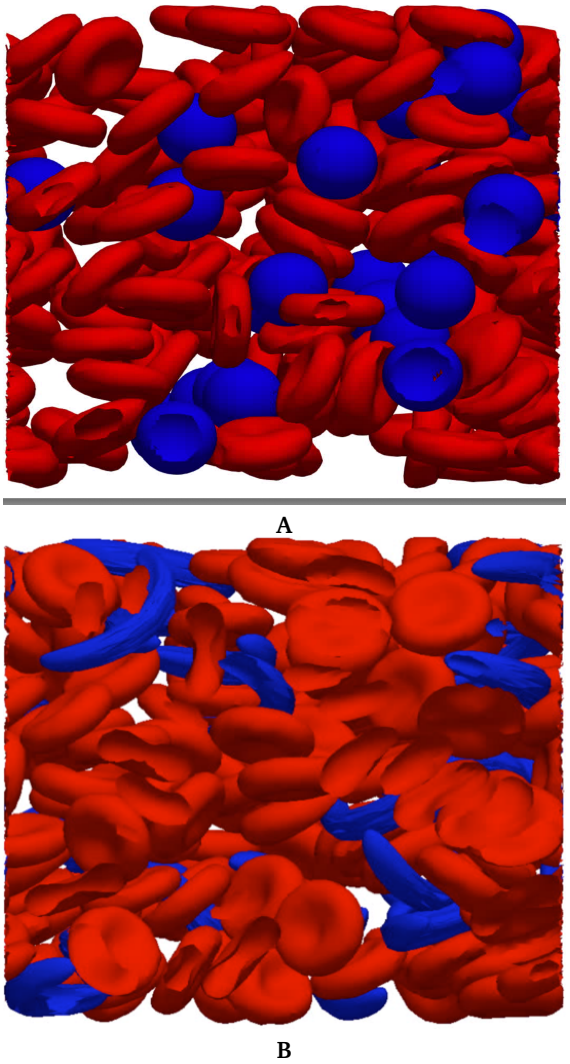


**Fig. 2** Snapshots of the sheared suspension of healthy RBC cells (red) and rigid particles or rigid sickled RBCs (blue). (A) 20% healthy RBCs and 5% rigid particles, and (B) 20% healthy RBCs and 5% rigid RBCs at 8 $s^{-1}$ shear rate.

In the DPD simulations, each of the five suspensions is sheared by a linear shear flow of shear rate 100 $s^{-1}$, 50 $s^{-1}$, 25 $s^{-1}$, 8 $s^{-1}$, and 5 $s^{-1}$, spanning a comparable range to the experiments. At a total volume fraction of 25%, the numerical resolutions are kept sufficiently high to prevent the particles and RBCs from overlapping each other in space. In addition we mimic the aggregation of RBCs due to their interactions with fibrinogen and globulins via an adhesion potential. We incorporate such adhesion interactions between RBC/RBC, RBC/particle, and particle/particle based on a Morse potential, which is described in detail in § 3.4. The adhesion energy density is given as $D = 9\ \mu J/m^2$ (Flormann *et al.* [39], Fedosov *et al.* [40]) for all the simulations unless otherwise

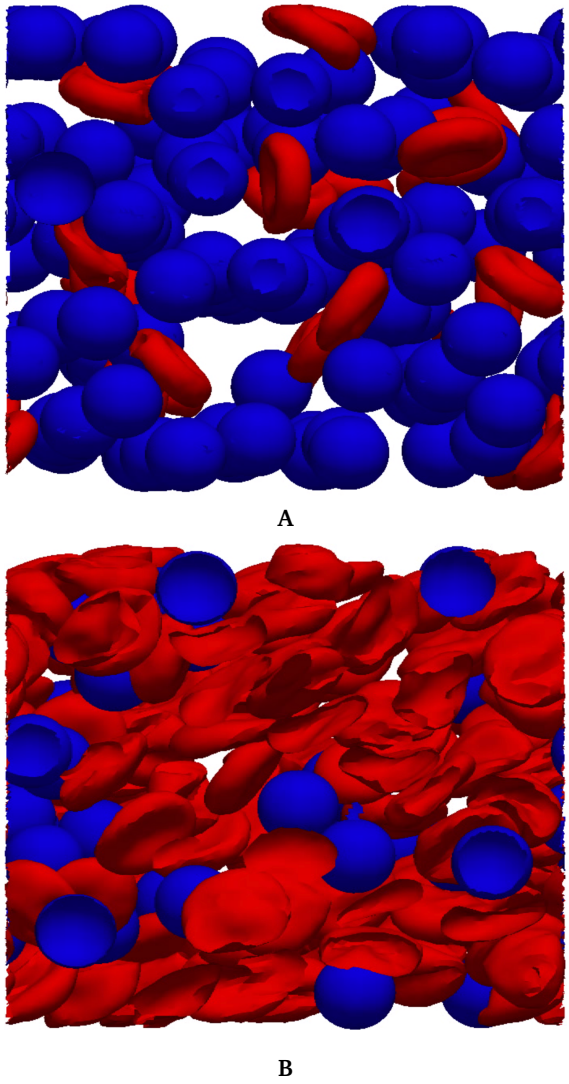


**Fig. 3** Snapshots of the sheared suspension of healthy RBC cells (red) and rigid particles or rigid sickled RBCs (blue). (A) 5% healthy RBCs and 20% rigid particles and (B) 20% healthy RBCs and 5% rigid particles at 100 $s^{-1}$ shear rate.

specified. Then, the average stress is calculated based on the virial stress using spatial and temporal averaging, and the effective suspension viscosity is obtained by dividing the stress by the shear rate (see §A.2 in the Appendix). The stress contributions due to the different components of the suspension, e.g., fluid, RBCs, rigid particles, etc., can be dissected as discussed in §A.6 in the Appendix. Snapshots of deformed individual cells and their interactions with other cells and rigid particles are shown in Figure 2. In the initial configuration, healthy RBCs have the same enclosed volume and biconcave shape, and are separated from each other and the rigid particles.

At low shear rates ($< 8\ s^{-1}$) and a concentration of 25% the RBCs translate and rotate like rigid bodies without observable deformation under the shear flow, although distortion has been observed for higher concentrations (50%) at low shear rates[41]. For the mixture of 5% particles and 20% RBCs with normal adhesion energy density between cells, we observed formation of rouleaux

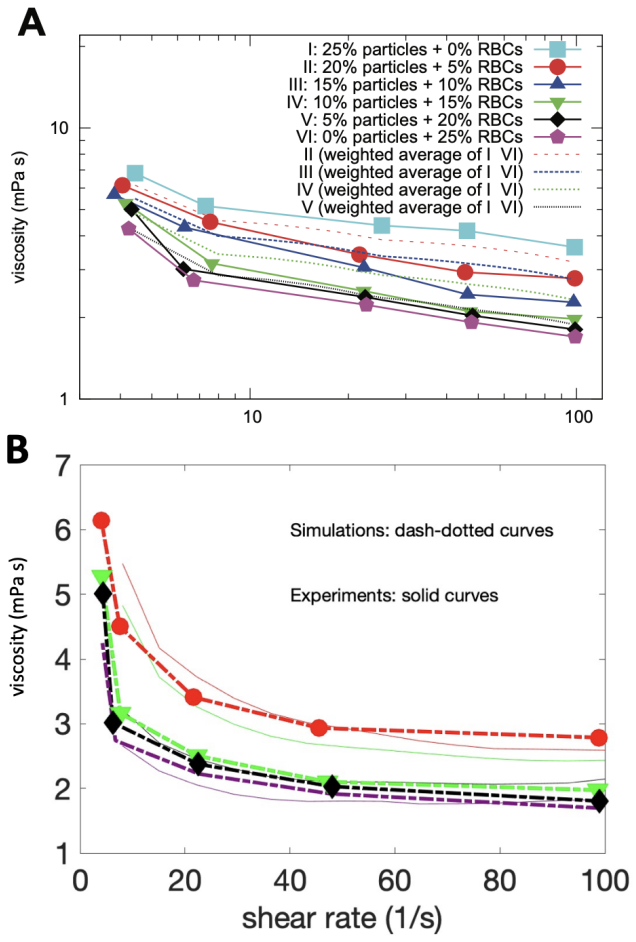


**Fig. 4** Numerically calculated viscosity as a function of shear rate, as determined by DPD simulations. (A) Suspension consisting of rigid particles and RBCs, with an adhesion energy density $D = 9\ \mu J/m^2$ between the particles. (B) Comparison with experimental data in Figure 1A for cases II, IV, V and VI.

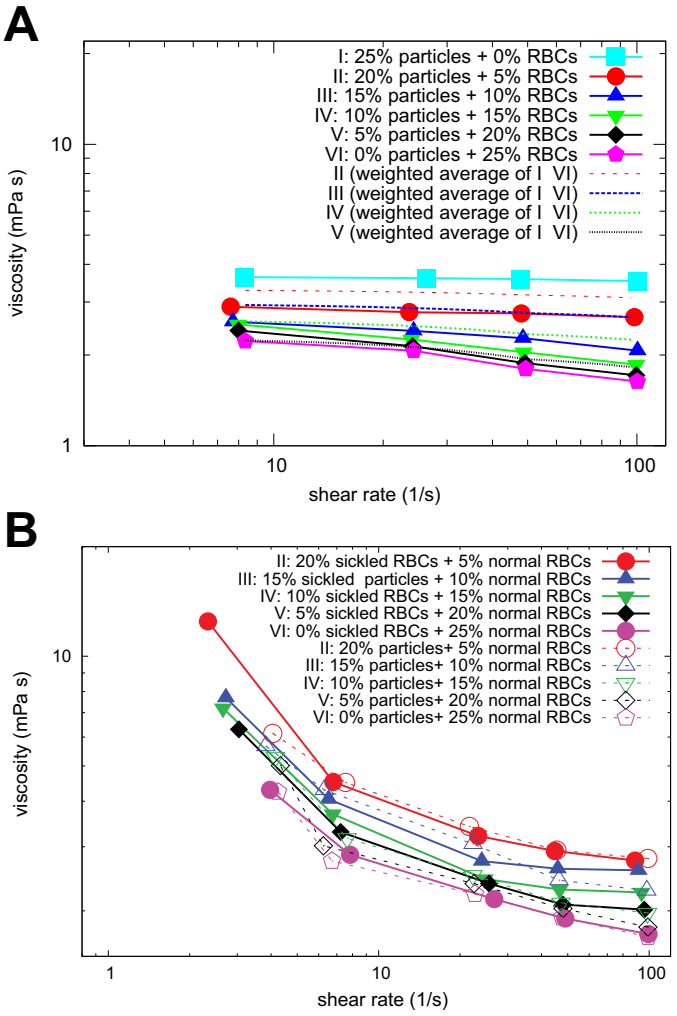


**Fig. 5** Numerically calculated viscosity as a function of shear rate, as determined by DPD simulations. (A) Suspension consisting of rigid particles and RBCs, without adhesion between the particles. (B) Suspension consisting of rigid sickle cells and healthy deformable RBCs by replacing the rigid particles in the simulations of Figure 4A with rigid sickle cells with the same surface area. The cases of rigid particles in Fig. 4A are shown as dashed lines.

of a few RBCs, as shown in Figure 2A and SI Movie 1. We observe similar behavior when we replace the rigid particles with the rigid sickled RBCs, shown in Figure 2B and SI Movie 2. For higher particle concentrations, as in Figure 3A, the RBCs can be strongly squeezed between rigid particles even under moderate shear rates ($\sim 25\ s^{-1}$). For higher shear rates ($\sim 100\ s^{-1}$), most of the RBCs are distorted as shown in Figure 3B. However, in our simulations, the RBCs are not elongated, nor do they tank-tread, unless the shear rate is increased to higher than $1000\ s^{-1}$. In summary, for the range of physiological shear rates we studied in the simulations, which was comparable to the experimental measurements, the adhesion and hydrodynamic interactions between the cells and particles are important, while the contributions from the cell deformation only become significant at higher shear rates.

We report the effective viscosity of the suspension as a function of the shear rate for the five different suspensions (labeled I-V), as presented in Figure 4. Figure 4A is with an adhesion energy density[39,40] $D = 9\ \mu J/m^2$. The reason for a significant increase in viscosity beyond 10% rigid particle fraction in Figure 4A is due to the strong nonlinear dependence of viscosity on rigid particle volume fraction beyond 10%, whereas there is a weaker dependence of viscosity on RBC volume fraction. This effect is clearly shown in[41]. Beyond 10% volume fraction, the viscosity of a suspension of rigid spheres increases exponentially while that of a normal RBC suspension increases much more slowly due to the deformability of RBCs. Therefore, replacing 5% RBCs by 5% rigid particles at a higher volume fraction (e.g. from green to blue curves in Figure 4A) will lead to more significant increase than that at a lower volume fraction (e.g. from black to green curves); in other words, the more the rigid particles the more non-linear is the increment in viscosity.

The comparison with the experimental measurements reported in Figure 1A is presented in Figure 4B. The viscosity increases with decreasing shear rate, and increases with increasing volume fraction of rigid particles (maintaining the total volume fraction fixed). Note that we studied an additional set of suspensions (case II, 15% particles + 10% RBCs, blue curve), which is missing in

the experimental data, and its viscosity is between cases I and III. Comparing with the experimental measurements, the main difference is that for case III (10% particles + 15% RBCs, green curve) the calculated viscosity is closer to case I (20% particles + 5% RBCs, red curve) in the experiments than in the simulations.

The discrepancies between green curves in Figure 4 might be due to some complicated features of the suspension in the experiments that were not captured in simulations. For example, the RBC population has a distribution of the surface-to-volume ratio, but this ratio is assumed to be constant in simulations, since every RBC has the same initial shape. One possibility for the viscosity jump at a lower rigid particle fraction in the experiments is due to the higher stress contribution from RBCs with lower surface-to-volume ratio in the RBCs population, while in simulations, because of the uniform surface-to-volume ratio, the viscosity jump occurs at a higher volume fraction. Another possibility is the buckling instability, which happens more abruptly in simulations than experiments, as mentioned by Lanotte et al.[16] to explain the discrepancies between modeling and experiments; the loss of the dimple happens abruptly in simulations highlighting a buckling instability, which is also confirmed experimentally by the long time scales (minutes) necessary for the population of stomatocytes to relax to a discocyte shape. The buckling instability may happen more abruptly in simulations than experiments so that the green curve is higher in experiments than the simulations, since the buckling leads to a softer response.

To further relate our study to sickle cell disease, we (1) turned off the adhesion between particles and RBCs (see Figure 5A) and (2) replaced the rigid particles in our simulations with rigid cells with the same surface area and with the same adhesion energy in Figure 5B). A simple way to ensure the same surface area for the rigid cells is to assume that the sickle RBCs are the same shape as the healthy RBCs but with a much larger bending stiffness. We note that given these conditions the volume fractions of the sickle cells are only approximate. Also, the lowest shear rate is 8 $s^{-1}$ instead of 5 $s^{-1}$. With this alternative mixture of rigid and soft particles, the results in Figure 5B show that the trends with the volume fraction of rigid sickle cells and shear rate are similar to those of rigid particles (dashed lines) from Figure 4A. Hence, we conclude that it is the rigidity of a fraction of cells, rather than their detailed shape, that has the most significant effect on the rheology. We note that the feature of pathologic shape versus pathologic stiffness may be important for understanding disease more generally, with the dominant effect likely to be pathologic stiffness (as also suggested by earlier SCA research, e.g.,[42]).

### 3.3 Model for a bimodal suspension of cells

In the literature on suspension mechanics, the shear viscosity of a suspension of rigid spheres of two different radii has been shown to be reduced from that of a monodisperse suspension of the same overall volume fraction due to crowding effects[43–46]; there is also recent work on suspensions of deformable particles[47]. Furthermore, such crowding effects produce more reduction in the shear viscosity as the total volume fraction of particles increases. When the rigid particles are replaced by capsules (with a membrane

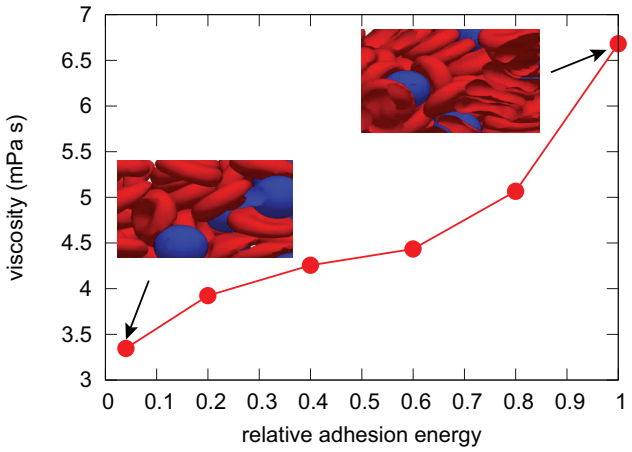


**Fig. 6** Predicted viscosity as a function of inter-particle adhesion energy density as calculated with DPD simulations. The adhesion energy density is normalized by $D = 9\ \mu J/m^2$. The suspension in the simulations consists of 15% RBCs and 10% particles with a shear rate of 5 $s^{-1}$.

that follows the so-called Skalak constitutive law), the capsule deformability is found to be responsible for reducing the shear viscosity of the suspension[48,49]. Furthermore, the shear viscosity of a bimodal suspension of capsules (of different bending rigidity, capsule size or excess area) can be well approximated by the weighted average viscosity[50]

$$\mu = (1 - R_\phi)\mu(R_\phi = 0) + R_\phi \mu(R_\phi = 1), \quad R_\phi \equiv \frac{\phi_{RBC}}{\phi}, \qquad (1)$$

where $0 \leq R_\phi \leq 1$ is the relative volume fraction of the capsules, which here is applied to the total volume fraction of the RBC suspension (for our work $0 \leq \phi_{RBC} \leq 25\%$). Here $\mu(R_\phi = 0)$ is the effective viscosity of the suspension with a total volume fraction $\phi = 25\%$ of all rigid particles (cases I in Figures 4A and B), and $\mu(R_\phi = 1)$ is for all healthy RBCs (cases VI in Figures 4A, B and C). The predictions of equation (1) are consistent with results in Figure 4A and Figure 5A (dashed lines), where we show that the weighted average of the shear viscosity of the RBC/particle suspension is a good approximation to predict the viscosity of the mixed suspension when the rigid particle volume fraction is smaller than the RBC volume fraction; the model is typically 10-30% higher than the simulations. Since the viscosity is shear rate dependent, the estimate of the viscosity of the mixed suspensions was performed for five different shear rates in the range (1–100/s) using Eq. 1 and the results are reported in Figure 4A and Figure 5A.

### 3.4 Computational prediction of the viscosity as a function of inter-particle adhesion

As a final aspect for characterizing the response of the suspension to shear flow, RBC aggregation has been shown to affect the effective viscosity of blood flow[21,51–53]; see, for example, Chien[54]. It is believed that the aggregation is due to interactions between RBCs and fibrinogen[55]. To mimic such RBC-protein interactions that lead to RBC aggregation, we introduce an adhesion potential[39,56] in the DPD simulations.

We used the same adhesion energy density between the vertices of all particles and RBCs in the DPD simulations, i.e., there were no differences in adhesion between RBC/RBC, RBC/particle and particle/particle. The effective adhesion energy density is given by the Morse potential,

$$U_{\text{Morse}} = D[1 - e^{-\alpha(r-r_e)}]^2, \quad (2)$$

where $D$ is the adhesion energy density, $r$ is the distance between two points, $r_e$ is the equilibrium distance, and $\alpha$ is a "softening" parameter. The corresponding adhesion force between two DPD particles is calculated as the derivative of adhesion energy density with respect to distance multiplied by the surface area of the cell membrane possessed by a DPD particle. For example, as the cell membrane with a total surface area of 135 $\mu$m$^2$ is represented by 500 DPD particles, each DPD particle possesses an area of 0.26 $\mu$m$^2$. We set $\alpha = 5.0$ and $r_e = 0.5$ $\mu$m.

We consider a suspension with 15% RBCs, 10% rigid particles and a shear rate of 5 s$^{-1}$. Experimental and computational data show that the adhesion energy density between healthy RBCs is about $1 - 10$ $\mu$J/m$^2$, while we set $D = 9$ $\mu$J/m$^2$ (Flormann *et al.* [39], Fedosov *et al.* [40]) in our DPD simulations. The dependence of the suspension viscosity on the relative adhesion energy density, which is normalized by $D = 9$ $\mu$J/m$^2$, is shown in Figure 6. The insets are snapshots of the suspension at different adhesion strengths. At low adhesion strength, RBCs do not aggregate and there is no evidence for cluster formation. For example, to have an increase in viscosity comparable to what is observed when changing from 5% to 10 % rigid particles, i.e., from 3.5 to 4.5 mPa s, according to Figure 6, the adhesion strength has to increase by twenty fold, which is unphysical. This result emphasizes the significant role of increased rigidity of a fraction of RBCs for increasing the viscosity of sickle blood.

## 4 Conclusions

We performed experiments and DPD simulations to show that there is an increase in the viscosity of SCA-affected blood, as compared to healthy blood, which allows identification of the approximate fraction of rigidified, i.e., diseased, cells, with a volume fraction as low as 5%, within a population of healthy deformable cells. Specifically, we are referring here to cases where not all cells are rigidified/affected by sickle cell anemia, a situation occurring for example after transfusions.. We studied suspensions of 25% total volume fraction (typical of SCA) containing healthy RBCs and including as low as 5% volume fraction of rigid particles or cells. In the DPD simulations we also adjusted the adhesion energy density between the particles and observed a general trend of increasing suspension viscosity with adhesion energy, similar to simulation results for a dilute suspension of vesicle doublets [57].

We note that a similar dependence to the trends reported here for the effective viscosity of a composite suspension of soft and rigid particles of comparable size has been observed for a bidisperse suspension of two distinct sizes of rigid particle [45,46]. At a given shear rate and a total particle volume fraction, the effective viscosity of such a bidisperse suspension increases with the volume fraction of the larger particle for sufficiently large volume fraction of the larger particle. This dependence is consistent with our finding that the effective viscosity of a mixture of rigid and deformable particles increases with the volume fraction of rigid particles. Also, colloidal suspensions that are mixtures of soft and hard particles have been exploited to tailor the Young modulus of soft composites [58–60]. However, the particles were colloidal, and the concentrations studied were very high and close to the glassy state, which is in contrast to our case where the particles were supracolloidal and in a "semi" dilute regime of concentration. In addition, in the colloidal soft-hard mixtures reported in the literature, the soft particles are usually made with a solid core and a surface coated by polymers, a feature that makes this system even more different from the one we considered in this paper.

Two results are worth emphasizing. (1) We have noted above that for the healthy RBCs, the effect of a small fraction of rigid particles on the suspension is as if the healthy cells are immersed in a solvent with a viscosity much higher than the plasma. Thus, our study raises the possibility that this increased viscosity from increased rigid cell fraction may lead to cytoskeletal damage or even hemolysis of the normal/transfused cells. (2) In addition, we have noted that our numerical simulations show that hydrodynamic interactions between the cells and particles are important, while the contributions from the cell deformation only become significant at higher shear rates. This general feature implies that cellular material properties themselves (e.g., bending modulus) are not as important as the hydrodynamic consequences of the altered material properties. We speculate that a possible implication is that plasma has a much more difficult time flowing between cells when one or both are stiffened. Further research on this topic could seek to understand whether the resistance the plasma experiences during flow may scale differently than changes in the material properties of a cell, e.g., does decreasing cellular rigidity by two times decrease the plasma drag by much less than two times and thus have a much lower than expected effect on suspension viscosity? (3) We also note that most of the increase in the viscosity of the sickled RBC suspensions, as compared to healthy RBC suspensions, is mostly due to the rigidity of the cells rather than their sickled shape, as indicated by our numerical simulations..

Moreover, our results suggest improved understanding is possible for blood transfusions and blood hyperviscosity syndrome [61]. For example, the results reported in this paper suggest estimates for how the transfusion of a certain amount of healthy blood can change the viscosity of the mixed blood in sickle cell patients. Thus, our study motivates a follow-up investigation exploring how variable rigidity of cells at a given rigid particle fraction would affect viscosity. For example, some experimental gene therapy treatments for sickle cell disease will partially lower the amount of hemoglobin polymer in a subset of cells, generating the equivalent of partially-rigid particles, though it is unclear whether reducing the cell stiffness by 50% will have a significant impact. Nevertheless, we speculate that understanding the rheological consequences of partial reduction in stiffness would be clinically relevant. Finally, we note that a simple blood transfusion recommended by current SCA guidelines (see `https://www.ncbi.nlm.nih.gov/pubmed/25203083`) in some clinical situations will result

in 20% of the RBCs being from a normal donor (healthy RBCs), and the other 80% the sickle cell patient's own cells that will stiffen when deoxygenated. This clinical situation is analogous to the experiments and simulations with 20% rigid cell volume fraction and 5% healthy (soft) cell volume fraction. Also, a chronic transfusion regimen or an RBC exchange procedure typically has a target roughly corresponding to a 30-40% rigid cell fraction, and a 60-70% healthy (soft) cell fraction, analogous to our 10% rigid particle and 15% normal RBC volume fraction experiments and simulations. The significant reduction in effective viscosity we find under these conditions is consistent with the stronger clinical efficacy of these more intense transfusion regimens (again see `https://www.ncbi.nlm.nih.gov/pubmed/25203083`).

## Conflicts of Interest

There are no conflicts of interest to declare.

## Acknowledgements

We thank the NIH for support via the National Heart, Lung, and Blood Institute, grant # R01HL132906 (to DKW and JMH with a subcontract to HAS). YNY is supported by NSF/DMS 1614863/1951600 and the Flatiron Institute, part of Simons Foundation. ZP and ZF are supported by NSF/CBET 1706436/1948347 and NSF/DMS 1951526. The authors thank Prof. Giovanna Tomaiuolo for helpful discussions concerning wall slip, particles and cells margination/migration.

# A Computational Modeling of the Rheology of Mixed Soft Red Blood Cells and Hard Particles

A coarse-grained molecular dynamics, dissipative particle dynamics (DPD), is applied to predict the shear-dependent viscosity of a suspension of mixed soft red blood cells and hard particles. First, we describe how to calculate the stress and viscosity of the fluid-RBC system. Second, we present details of the DPD method and the red blood cell (RBC) model, including the membrane viscosities and the elasticities of both the lipid-bilayer and the cytoskeleton. There are two alternative approaches to model the hard particles. First, the hard particles can be modeled using the RIGID package in LAMMPS[62]. Second, the hard particles can be modeled as the same way as the soft RBCs, except their geometries are given as perfectly spheres. Since the volume and surface areas of these spheres are conserved in our simulations, they are not able to deform and behavior as rigid bodies. We adopted the second approach for the hard spherical particles and the first approach for the rigid sickled cells.

### A.1 Calculations of stress and viscosity of the particle system

We model both the RBC membranes and fluid using DPD "particles". To calculate the stress of a region, we define the stress at a particle first and then perform the spatial and temporal averaging. The viscosity is obtained as the calculated shear stress divided by the shear rate.

### A.2 Stress defined at a particle

The stress $\boldsymbol{\sigma}^I$ of a particle I is defined as the virial stress as[28,30]

$$\begin{aligned}\sigma^I_{ab} &= -\frac{1}{V^{(I)}}\Bigg[mv_a v_b + \frac{1}{2}\sum_{n=1}^{N_{pair}}(r_a^{(1)}F_b^{(1)} + r_a^{(2)}F_b^{(2)}) \\ &\quad + \frac{1}{2}\sum_{n=1}^{N_{bond}}(r_a^{(1)}F_b^{(1)} + r_a^{(2)}F_b^{(2)}) \\ &\quad + \frac{1}{3}\sum_{n=1}^{N_{angle}}(r_a^{(1)}F_b^{(1)} + r_a^{(2)}F_b^{(2)} + r_a^{(3)}F_b^{(3)}) \\ &\quad + \frac{1}{4}\sum_{n=1}^{N_{dihedral}}(r_a^{(1)}F_b^{(1)} + r_a^{(2)}F_b^{(2)} + r_a^{(3)}F_b^{(3)} + r_a^{(4)}F_b^{(4)})\Bigg] \\ &\quad + \sum_{n=1}^{N_{fix}} r_a^{(I)}F_b^{(I)} \end{aligned} \tag{3}$$

where subscripts $a$ and $b$ take on values $x, y, z$ to generate the 6 components of the symmetric stress tensor, and $V^{(I)}$ is the volume of the particle $I$. The first term is a kinetic energy contribution for particle $I$ with mass $m$ and velocity $v$. The second term is a pairwise energy contribution over the $N_{pair}$ neighbors of particle $I$, $\mathbf{r}^{(1)}$ and $\mathbf{r}^{(2)}$ are the positions of the two particles in a pairwise interaction, and $\mathbf{F}^{(1)}$ and $\mathbf{F}^{(2)}$ are the forces on the two particles resulting from the pairwise DPD interaction, which represents the hydrodynamic contribution. The third term is a bond contribution of similar form for the $N_{bond}$ bonds that involve particle $I$ and represents the shear elasticity contribution from the cytoskeleton. There are similar terms for the $N_{angle}$ angle and $N_{dihedral}$ dihedral interactions involving particle $I$, which represent the contributions from the area and volume conservation and the bending rigidity of the lipid bilayer. Finally, there is a term for the LAMMPS 'fixes' that apply internal constraint forces to atom. In the current study, the fix rigid commands for modeling rigid particles using the RIGID package[62] contribute to this term.

### A.3 Mean stress by spatial and temporal averaging

The mean stress $\bar{\boldsymbol{\sigma}}$ within a region can be calculated as

$$\bar{\sigma}_{ab} = \frac{\sum_{I=1}^{N_{particles}} \sigma^I_{ab} V^{(I)}}{\sum_{I=1}^{N_{particles}} V^{(I)}} = \frac{\sum_{I=1}^{N_{particles}} \sigma^I_{ab} V^{(I)}}{V}, \tag{4}$$

where $V$ is the volume of the region and as before $V^{(I)}$ is the volume of the particle $I$. Then this spatial mean stress is also averaged in time after initial transient steps to obtain the final shear stress to calculate the viscosity.

### A.4 Dissipative particle dynamics model of healthy and sickled red blood cells

We applied the DPD model of red blood cells we developed before to predict the viscosity[63,64]. The DPD method is a particle-based mesoscopic simulation technique that allows modeling of

fluids and soft matter. A DPD system is represented by $N$ particles, which interact through pairwise effective potentials and move according to Newton's second law[26,27]. In a DPD simulation, a particle represents the center of mass in a cluster of atoms or molecules, and the position and momentum of the particle are updated in a continuous phase but spaced at discrete time steps. Particles $i$ and $j$ at positions $r_i$ and $r_j$ interact with each other *via* pairwise conservative $\mathbf{F}^C$, dissipative $\mathbf{F}^D$, and random forces, $\mathbf{F}^R$, which are given by

$$F_{ij}^C = a_{ij}\omega(r_{ij})\mathbf{n}_{ij}, \quad (5a)$$

$$F_{ij}^D = -\gamma\omega^2(r_{ij})(\mathbf{n}_{ij}\cdot\mathbf{v}_{ij})\mathbf{n}_{ij}, \quad (5b)$$

$$F_{ij}^R = \sigma\omega(r_{ij})\zeta_{ij}\Delta t^{-1/2}\mathbf{n}_{ij}, \quad (5c)$$

where $\mathbf{r}_{ij} = \mathbf{r}_i - \mathbf{r}_j$, $r_{ij} = |\mathbf{r}_{ij}|$, $\mathbf{n}_{ij} = \mathbf{r}_{ij}/r_{ij}$, and $\mathbf{v}_{ij} = \mathbf{v}_i - \mathbf{v}_j$. The coefficients $a_{ij}$, $\gamma$ and $\sigma$ define, respectively, the strength of conservative, dissipative and random forces. In addition, $\zeta_{ij}$ is a random number with zero mean and unit variance, and $\Delta t$ is the time step. The weight function $\omega(r_{ij})$ is given by

$$\omega\left(r_{ij}\right) = \begin{cases} 1 - r_{ij}/r_c & r_{ij} < r_c \\ 0 & r_{ij} \geq r_c \end{cases} \quad (6)$$

where $r_c$ is a cutoff radius, which gives the extent of the interaction range. In the DPD method, the dissipative force and the random force act as a heat sink and source respectively, and the combined effect of the two forces acts a thermostat. Also, a common choice of the soft repulsion for the conservative force permits us to use larger integration time steps than are usually allowed by the molecular dynamics (MD) simulation technique, thus DPD is a simple but efficient simulation method that correctly represents hydrodynamic interactions.

In the RBC model, the membrane is modeled by a two-dimensional triangulated network with $N_v$ vertices, as shown in Fig. S1A, where each vertex is represented by a DPD particle. $N_v = 500$ is used for the current study. The lipid-bilayer has no shear stiffness but only bending stiffness and a very large local area stiffness, whereas the inner layer (cytoskeleton) has no bending stiffness but a large shear stiffness. The potential energy of the RBC membrane including these two different components is written as

$$U = U_s + U_b + U_{a+v} + U_{int}, \quad (7)$$

where $U_s$ is the spring's potential energy from the cytoskeleton, given by

$$U_s = \sum_{j\in 1\ldots N_s}\left[\frac{k_{\mathrm{B}}Tl_m(3x_j^2 - 2x_j^3)}{4p(1-x_j)} + \frac{k_p}{(n-1)l_j^{n-1}}\right], \quad (8)$$

where $N_s$ is the number of springs, $l_j$ is the length of the spring $j$, $l_m$ is the contour length, $x_j = l_j/l_m$, $p$ is the persistence length, $k_{\mathrm{B}}$ is the Boltzmann constant, $T$ is the temperature, $k_p$ is the spring constant, and $n$ is a parameter. The first term is a worm-like chain (WLC) model[65] while the second term is a repulsive force term. Note that in the finite-element simulations[66], a simple functional form $C/A$ is used, where $C$ is a constant and $A$ is the area of the corresponding triangle in the spectrin network. The isotropic mean stress for an equilateral triangle in the network is given as

$$\bar{T} = -\frac{3lf_{\mathrm{WLC}}(l)}{4A} - \frac{C}{A^2}, \quad (9)$$

where $l$ is the length of the spectrin link, $f_{\mathrm{WLC}}(l)$ is the force of the WLC model and $A = \sqrt{3}l^2/4$. In our simulations, we have $\bar{T} = 0$ for the lipid-bilayer.

Also, $U_b$ is the bending energy from the lipid-bilayer, given by

$$U_b = \sum_{j\in 1\ldots N_s} k_b\left[1 - \cos(\theta_j - \theta_0)\right], \quad (10)$$

where $k_b$ is the bending coefficient and $k_b = 2k_c/\sqrt{3}$, where $k_c$ is the bending stiffness of the bilayer. Also, $\theta_j$ is the instantaneous angle between two adjacent triangles as shown in Fig. S1*B,C*, and $\theta_0$ is the spontaneous angle, which is set to zero in our simulations. Finally, $U_{a+v}$ corresponds to the area and volume conservation constraints from the lipid-bilayer, given by

$$U_{a+v} = \sum_{j\in 1\ldots N_t}\frac{k_l(A_j - A_0)^2}{2A_0} + \frac{k_v(V^{tot} - V_0^{tot})^2}{2V_0^{tot}}, \quad (11)$$

where $N_t$ is the number of triangles in the lipid-bilayer, $A_j$ is the instantaneous triangle area as shown in Fig. S1*B,C*, and $A_0$ is the initial triangle area. $V^{tot}$ is the current total RBC volume, while $V_0^{tot}$ is the initial total RBC volume. Also, $k_l$ and $k_v$ are the bilayer local area constraint coefficient and global volume constraint coefficient, respectively.

The parameters in Eq. 9 are chosen to give an initial shear modulus of 6 pN/$\mu$m. The bending stiffness $k_c$ is set to 50 $k_BT$ in Eq. 10. $k_v = 5000$ and $k_l = 5000$ in DPD units are used in Eq. 11 to enforce the area and volume conservation.

To generate the shapes of sickled red blood cells studied in Fig. 2B, we applied stretching forces at the anchoring points to mimic the force due to intracellular hemoglobin polymerization by following the approach in[29]. The sickled cells are then modeled as rigid bodies using the rigid body package in LAMMPS.

### A.5 Effect of adhesion

We apply the Morse potential between the membrane DPD particles to consider the adhesion between RBCs. The Morse potential is given as

$$U_{\mathrm{Morse}} = D(1 - e^{-\alpha(r-r_e)})^2, \quad (12)$$

where $D$ is the adhesion energy, $r$ is the current distance, $r_e$ is the equilibrium distance, and $\alpha$ is a softening parameter.

### A.6 Dissecting the contributions to the shear stress and viscosity by computational modeling

We further analyzed the shear stress by dissecting it into different contributions from hydrodynamic interactions, RBC cytoskeleton shear deformation, RBC bilayer deformation, and stress from rigid particles, as shown in Fig. S2. Since the viscosity is calculated as shear stress divided by shear rate, this also shows how different components contribute to the viscosity. This calculation

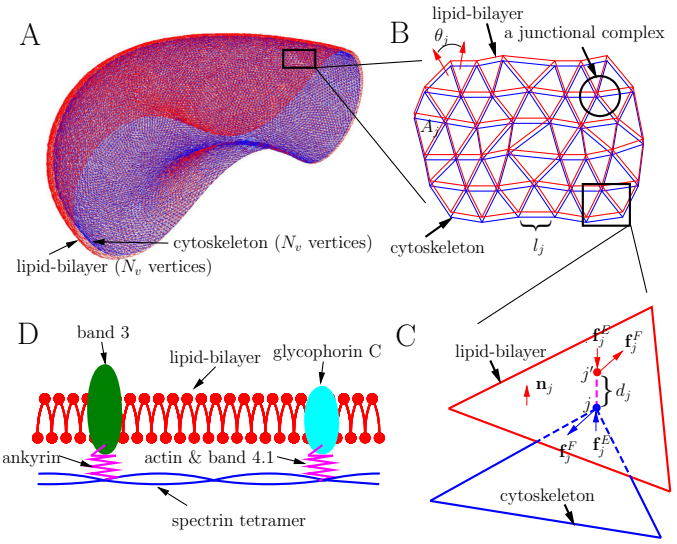


Figure S1: Multiscale model of the red blood cell membrane[63]. (*A*) Two-component DPD model of the whole cell. (*B*) Local triangular networks of the two-component model: $l_j$ is the spring length of the cytoskeleton; $\theta_j$ is the instantaneous angle between two adjacent triangles on the bilayer; and $A_j$ is the triangle area. (*C*) Normal and tangential interactions between the lipid-bilayer and the cytoskeleton. $j'$ is the projection point on the lipid-bilayer of vertex $j$ on the cytoskeleton; $d_j$ is the distance between point $j$ and point $j'$; $\mathbf{f}_j^F$ is the tangential friction interaction force, while $\mathbf{f}_j^E$ is the normal elastic interaction force; $\mathbf{n}_j$ is the normal direction vector of the bilayer triangle. (*D*) Physical picture of the local bilayer–cytoskeletal interaction. Although there are two kinds of interactions in each junctional complex, including the major connections *via* band-3 and ankyrin and the secondary connections *via* actin, glycophorin C and band-4.1, we consider them together as an effective bilayer–cytoskeletal interaction in one junctional complex and model it as a normal elastic force and a tangential friction force. The vertical damping force $\mathbf{f}_j^D$ and the random force $\mathbf{f}_j^R$ are not shown in the figure for clarity.

is achieved using the stress/tally command in the TALLY package in LAMMPS[30]. Specifically, we calculated stress contributions from the pair and bonded interactions (Eq. 3 in the Appendix) between two groups of particles (these two groups can be identical) and summed them to get the results in Fig. S2, which shows that with a fixed total volume fraction (25%) but increasing rigid particle volume fraction, the percent contribution from rigid particles to stress increases as expected. However, the percentage contribution of hydrodynamic interaction decreases slightly (Fig. S2 B), because the total shear stress of the 5% RBC case is higher than the 20% RBC case under the same shear rate (100 $s^{-1}$). Our results show that the absolute value of the hydrodynamic stress is slightly higher in the 5% RBC case than in the 20% RBC case (Fig. S2 A) although its percent contribution is lower. Our results also show that the main stress contribution of RBCs is from their cytoskeletal deformation rather than the lipid bilayer. The latter includes bilayer bending, local area conservation, and global volume conservation imposed by the bilayer (Equations 10 and 11 in the Appendix). The adhesive contribution in this case under a shear rate of 100/s is quite small and is included in the contributions of RBCs (bilayer) and rigid particles. More details on how the stress is calculated is given in §A.2.

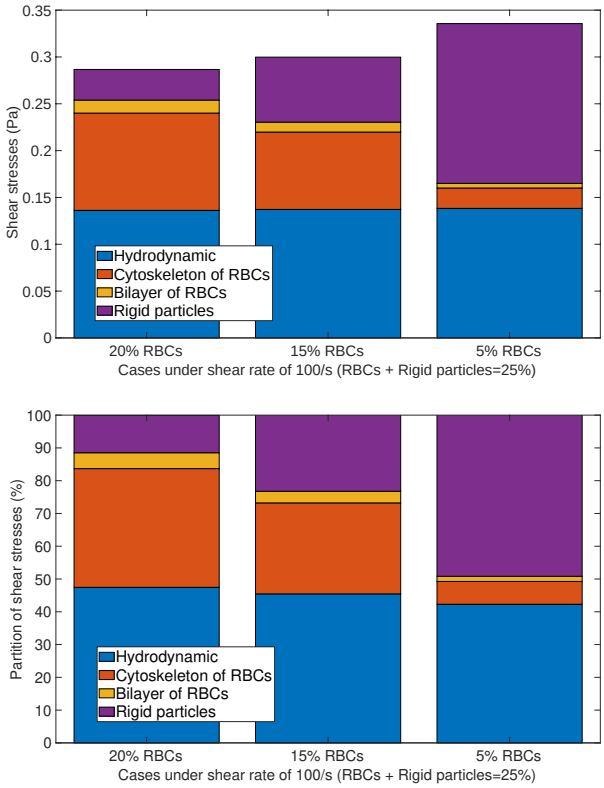


Figure S2: Partition of the shear stresses contributed by hydrodynamic interaction, cytoskeletal shear stress of RBCs, bilayer stress of RBCs, and the stress from the rigid particles for cases with a shear rate of 100 $s^{-1}$. (A) The absolute values of stress contributions. (B) The percent stress contributions.

## Notes and references


1 A. Viallat and M. Abkarian, *Int. J. Laboratory Hematology*, 2014, **36**, 237–243.

2 G. Tomaiuolo, *Biomicrofluidics*, 2014, **8**, 051501.

3 G. Tomaiuolo, A. Carciati, S. Caserta and S. Guido, *Rheol. Acta*, 2016, **55**, 485–495.

4 M. Abkarian, M. Faivre and A. Viallat, *Phys. Rev. Lett.*, 2007, **98**, 188302.

5 M. Abkarian, M. Faivre, R. Horton, K. Smistrup, C. A. Best-Popescu and H. A. Stone, *Biomed. Mater.*, 2008, **3**, 034011.

6 B. Kaoui, G. Biros and C. Misbah, *Phys. Rev. Lett.*, 2009, **18**, 188101.

7 G. Tomaiuolo, M. Simeone, V. Martinelli, B. Rotoli and S. Guido, *Soft Matt.*, 2009, **5**, 3736.

8 D. A. Fedosov, M. Peltomaki and G. Gompper, *Soft Matt.*, 2014, **10**, 4258–4267.

9 O. Baskurt and H. Meiselman, *Seminars in Thrombosis and*

*Hemostasis*, Thieme Medical Publishers, Inc., New York, 2003, pp. 435–450.
10 J. Horner, M. Armstrong, N. Wagner and A. Beris, *J. Rheology*, 2018, **62**, 577–591.
11 M. Armstrong, J. Horner, M. Clark, M. Deegan, T. Hill, C. Keith and L. Mooradian, *Rheologica Acta*, 2018, **57**, 705–728.
12 J. S. Horner, M. J. Armstrong, N. J. Wagner and A. N. Beris, *J. Rheology*, 2019, **63**, 799–813.
13 A. N. Beris, J. S. Horner, S. Jariwala, M. Armstrong and N. J. Wagner, *Soft Matt.*, 2021.
14 D. A. Fedosov, H. Noguchi and G. Gompper, *Biomech. Model Mechanobiol.*, 2014, **13**, 239–258.
15 J. Dupire, M. Abkarian and A. Viallat, *Soft Matt.*, 2015, **11**, 8372–8382.
16 L. Lanotte, J. Mauer, S. Medez, D. A. Fedosov, J.-M. Fromental, V. Claveria, F. Nicoud, G. Gompper and M. Abkarian, *Proc. Nat. Acad. Sci.*, 2016, **113**, E8207.
17 T. Secomb, *Annual Review of Fluid Mechanics*, 2017, **49**, 443–461.
18 D. K. X. Lu, D.K. Wood and J. Higgins, *Biophysical J.*, 2016, **110**, 2752–2758.
19 J. H. X. Lu, A. Chaudhury and D. Wood, *American Journal of Hematology*, 2018, **93**, 1227–1235.
20 S. Chien, S. Usami, R. J. Dellenback and M. I. Gregersen, *Science*, 1967, **157**, 827–831.
21 S. Chien, S. Usami, R. J. Dellenback, M. I. Gregersen, L. B. Nanninga and M. M. Guest, *Science*, 1967, **157**, 829–831.
22 I. V. Pivkin and G. E. Karniadakis, *Phys. Rev. Lett.*, 2008, **101**, 118105.
23 D. A. Fedosov, B. Caswell and G. E. Karniadakis, *Biophys. J.*, 2010, **98**, 2215–2225.
24 D. A. Fedosov, B. Caswell and G. E. Karniadakis, *Comput. Meth. Appl. Mech. Eng.*, 2010, **199**, 1937–1948.
25 M. A. Panteleev, N. Korin, K. D. Reesink, D. L. Bark, J. M. E. M. Cosemans, E. E. Gardiner and P. H. Mangin, *Journal of Thrombosis and Haemostasis*, 2021, **19**, 588–595.
26 P. J. Hoogerbrugge and J. M. Koelman, *Europhys Lett.*, 1992, **19**, 155–160.
27 R. D. Groot and P. B. Warren, *J. Chem. Phys.*, 1997, **107**, 4423–4435.
28 D. J. Tildesley and M. P. Allen, *Computer Simulation of Liquids*, Oxford Press, 2017.
29 H. Lei and G. E. Karniadakis, *Biophys. J.*, 2012, **102**, 185–194.
30 S. Plimpton, *J. Comp. Phys.*, 1995, **117**, 1–19.
31 M. Brust, C. Schaefer, R. Doerr, L. Pan, M. Garcia, P. E. Arratia and C. Wagner, *Physical Review Letters*, 2013, **110**, 078305.
32 N. Mohandas and E. A. Evans, *Annu. Rev. Biophys. Biomol. Struct.*, 1994, **23**, 787–818.
33 C. J. Pipe, T. S. Majmudar and G. H. McKinley, *Rheol. Acta*, 2008, **47**, 621–642.
34 X. Zhang, C. Caruso, W. A. Lam and M. D. Graham, *Phys. Rev. Fluids*, 2020, **5**, 053101.
35 A. Kumar and M. D. Graham, *Soft Matt.*, 2012, **8**, 10536.
36 Q. M. Qi and E. S. G. Shaqfeh, *Phys. Rev. Fluids*, 2017, **2**, 093102.
37 R. D'Apolito, G. Tomaiuolo, F. Taraballi, S. Minardi, D. Kirui, X. Liu, A. Cevenini, R. Palomba, M. Ferrari, F. Salvatore, E. Tasciotti and S. Guido, *Journal of Controlled Release*, 2015, **217**, 263–272.
38 R. Fahreaus and T. Lindqvist, *The American Journal of Physiology*, 1931, **96**, 562–568.
39 D. Flormann, O. Aouane, L. Kaestner, C. Ruloff, C. Misbah, T. Podgorski and C. Wagner, *Scientific Reports*, 2017, **7**, 7928.
40 D. A. Fedosov, W. Pan, B. Caswell, G. Gompper and G. E. Karniadakis, *Proceedings of the National Academy of Sciences*, 2011, **108**, 11772–11777.
41 H. Goldsmith, *Theoretical and Applied Mechanics, Proc. 13th IUTAM Congress*, Springer, New York, 1972, pp. 85–103.
42 H. Hiruma, C. Noguchi, N. Uyesaka, S. Hasegawa, E. Blanchette-Mackie, A. Schechter and G. Rodgers, *Am. J. Hematol.*, 1995, **48**, 19–28.
43 R. J. Farris, *Transactions of the Society of Rheology*, 1968, **12**, 281–301.
44 A. Doerr, A. Sadiki and A. Mehdizadeh, *J. Rheology*, 2013, **57**, 743.
45 S. A. Faroughi and C. Huber, *Phys. Rev. E*, 2014, **90**, 052303.
46 C. I. Mendoza, *Rheol. Acta*, 2017, **56**, 487–499.
47 M. Rosti, L. Brandt and D. Mitra, *Phys. Rev. Fluids*, 2018, **3**, 012301.
48 J. R. Clausen and C. K. Aidun, *Phys. Fluids*, 2010, **22**, 123302.
49 J. R. Clausen, D. A. R. Jr. and C. K. Aidun, *J. Fluid Mech.*, 2011, **685**, 202–234.
50 H. Ito, D. Matsunaga and Y. Imai, *Phys. Rev. Fluids*, 2019, **4**, 113601.
51 S. Chien, L. A. Sung, S.Kim, A. M. Burke and S. Usami, *Microvascular Research*, 1977, **13**, 327–333.
52 D. A. Fedosov, H. Lei, B. Caswell, S. Suresh and G. E. Karniadakis, *PLoS Comput. Biol.*, 2011, **7**, e1002270.
53 M. Abbasi, A. Farutin, C. Misbah, H. Ez-Zahraouy and A. Benyoussef, *Phys. Rev. Fluids*, 2021, **6**, 023602.
54 S. Chien, *Science*, 1970, **168**, 977–979.
55 A. N. Semenov, A. E. Lugovtsov, E. A. Shirshin, B. P. Yakimov, P. B. Ermolinskiy, P. Y. Bikmulina, D. S. Kudryavtsev, P. S. Timashev, A. V. Muravyov, C. Wagner, S. Shin and A. V. Priezzhev, *Biomolecule*, 2020, **10**, 1448.
56 E. Javadi and S. Jamali, *Soft Matt.*, 2021, **17**, 8446–8458.
57 B. Quaife, S. Veerapaneni and Y.-N. Young, *Phys. Rev. Fluids*, 2019, **4**, 103601.
58 D. Truzzolillo, D. Marzi, J. Marakis, B. Capone, M. Camargo, A. Munam, F. Moingeon, M. Gauthier, C. N. Likos and D. Vlassopoulos, *Phys. Rev. Lett.*, 2013, **111**, 208301.
59 D. Marzi, B. Capone, J. Marakis, M. Merola, D. Truzzolillo, L. Cipelletti, F. Moingeon, M. Gauthier, D. Vlassopoulos, C. Likos and M. Camargo, *Soft Matter*, 2015, **11**, 8296–8312.
60 M. Merola, D. Parisi, D. Truzzolillo, D. Vlassopoulos, V. Deepak and M. Gauthier, *J. Rheology*, 2018, **62**, 63–79.

61 E. Javadi, Y. Deng, G. E. Karniadakis and S. Kamali, *Biophys. J.*, 2021, **120**, 2723–2733.
62 H. Kamberaj, R. J. Low and M. P. Neal, *J. Chem. Phys.*, 2005, **122**, 224114.
63 Z. Peng, X. Li, I. V. Pivkin, M. Dao, G. E. Karniadakis and S. Suresh, *Proceedings of the National Academy of Sciences*, 2013, **110**, 13356–13361.
64 I. V. Pivkin, Z. Peng, G. E. Karniadakis, P. A. Buffet, M. Dao and S. Suresh, *Proceedings of the National Academy of Sciences*, 2016, **113**, 7804–7809.
65 D. E. Discher, D. H. Boal and S. K. Boey, *Biophys. J.*, 1998, **75**, 1584–1597.
66 Z. Peng, R. Asaro and Q. Zhu, *Phys. Rev. E*, 2010, **81**, 031904.

## Author Contributions

We strongly encourage authors to include author contributions and recommend using CRediT for standardised contribution descriptions. Please refer to our general author guidelines for more information about authorship.

## Conflicts of interest

There are no conflicts to declare. Antonio Perazzo is an employee of Novaflux Inc. and Advanced BioDevices LLC. The views expressed in this article are those of the authors and do not necessarily reflect the position or policy of Novaflux Inc. and Advanced BioDevices LLC.